


Exploration of the spin-phonon coupling in the noncollinear antiferromagnetic antiperovskite Mn_3NiN


L. Florez-Gomez^{1,2}

¹*School of Physics, FICOMACO Research Group, Universidad Industrial de Santander, Carrera 27 Calle 09, 680002, Bucaramanga, Colombia. and*

²*Centro de Investigación y Estudios Avanzados del IPN - CINVESTAV-Querétaro, MX-76230, Querétaro, México.*

W. Ibarra-Hernandez³ 

³*Facultad de Ingeniería, Benemérita Universidad Autónoma de Puebla, Apartado Postal J-39, Puebla, Pue. 72570, México.*

A. C. Garcia-Castro⁴ *

⁴*School of Physics, CIMBIOS Research Group, Universidad Industrial de Santander, Carrera 27 Calle 09, 680002, Bucaramanga, Colombia.*

Antiferromagnetic antiperovskites, of the form Mn_3BN ($B = \text{Ni}, \text{Cu}, \text{Zn}, \text{Sn}, \text{Ir}, \text{and Pt}$), have shown an outstanding behavior in which, giant negative thermal expansion and chiral magnetic structures are intertwined. As such, aiming to shed light on the magnetostructural behavior, related to the magnetic ordering and structure of this type of materials, we studied by theoretical first-principles calculations the spin-phonon coupling in the Manganese-based antiperovskite Mn_3NiN , as a prototype in the Mn_3BN family. We found a strong spin-lattice coupling by means of the understanding of the phonon-dispersion curves obtained when including the chiral noncollinear magnetic structure. To do so, we highlight the importance of the exchange-correlation scheme selected and its influence on the electronic, structural, and vibrational degrees of freedom. Finally, we found two unstable vibrational modes at the M - and R -points when the magnetic ordering is switched to ferromagnetic from the chiral Γ_{4g} and Γ_{5g} . The latter coupling was observed as a key signature of the strong spin-lattice interaction.

DOI:

I. INTRODUCTION

Perovskite oxides, and perovskite structures in general (*i.e.* ABX_3), have been in the center of debate and development in the condensed matter field with phenomena ranging from multiferroism and magnetoelectricity [1–5] to applications and development in solar cells with hybrid-perovskites [6–8]. More recently, an associated family of materials has caught the attention of the scientific community due to the multifunctional character of its properties that cover, for example, anomalous Hall effect [9], superconductivity [10–12], novel batteries [13, 14], ferroelectricity [15], among other functionalities. This family of materials is known as antiperovskite, or inversed-perovskite (*i.e.* A_3BX) [16, 17], in which, the electrostatic balance and the oxidation site occupation is reversed with respect to the known perovskites [18]. In the antiperovskites, the anionic sites occupy the octahedral center, instead of the corners, and the cationic metal transition occupies the corners, instead of the octahedral center, forming the XA_6 octahedra. This change in coordination and atomic occupations give rise to astonishing novel properties. For instance, when magnetically active cations are placed at the A -sites to form the octahedra, added to the triangular geometric coordination of

the magnetic sites, a magnetic frustration is induced resulting in chiral noncollinear antiferromagnetic orderings [19]. This fascinating magnetic phenomenon is associated with the observed barocaloric response [20], large piezomagnetic behavior [21–24], topological anomalous Hall effect that can be controlled electrically [25, 26], and spin-torque switching [27]. Undoubtedly, the control of all of the latter effects is highly desirable when designing novel and efficient noncollinear spintronics controlled by external electric fields [28]. Some efforts have demonstrated the possible control of the magnetic ordering by the application of biaxial strain in thin films [29]. Moreover, intertwined magnetic and structural transitions are expected to occur as demonstrated by M. Wu *et al.* [30]. Additionally, the negative thermal expansion observed in the Mn_3BN family [31–33] is a signature of the strong magnetostructural coupling in this class of materials. For example, in their perovskite oxides counterparts, the magnetostructural coupling [34, 35] can induce tangible electric polarization, as in the case of the SrMnO_3 . Thus, such materials are driven to a multiferroic state thanks to their strong spin-phonon coupling assisted by epitaxial strain [36]. Consequently, when all the phenomena above are considered, the investigation of the phonon spectra and their coupling with the magnetic orderings can shed light on the physics hidden in these antiferromagnetic antiperovskites.

In this paper, we theoretically study, from first-

* acgarcia@uis.edu.co

principles calculations, the magnetostructural coupling by exploring the spin and vibrational degrees of freedom in the Mn_3NiN antiferromagnetic antiperovskite, as a prototype among its family. Moreover, we performed a careful analysis of the influence of the exchange-correlation on-site Coulomb U term into the physics behind the spin-phonon coupling and the electronic structure in this antiperovskite. This paper is organized as follows: In Section II are presented all the computational details and the theoretical approaches used in the analysis of this work. In Section III are shown the obtained results and the associated analysis related to the vibrational landscape of the Mn_3NiN noncollinear antiferromagnetic antiperovskite. Finally, in Section IV we highlight our conclusions and perspectives in regards to the strong magnetostructural response observed in Mn_3NiN .

II. COMPUTATIONAL DETAILS

We performed first-principles calculations within the density-functional theory (DFT) [37, 38] approach by using the VASP code (version 5.4.4) [39, 40]. The projected-augmented waves, PAW [41, 42] scheme was used to represent the valence and core electrons. The electronic configurations considered in the pseudo-potentials as valence electrons are Mn: ($3p^6 3d^5 4s^2$, version 02Aug2007), Ni: ($3p^6 3d^8 4s^2$, version 06Sep2000), and N: ($2s^2 2p^3$, version 08Apr2002). The exchange-correlation, E_{xc} , was represented within the generalized gradient approximation, GGA-PBESol parametrization [43], and the E_{xc} of the d -electrons was corrected through the DFT+ U approximation within the Liechtenstein formalism [44]. We used a Coulomb on-site value of $U = 2.0$ eV parameter. The latter optimized to reproduce the experimentally observed lattice parameter. Also, a metaGGA formalism [45], within the SCAN implementation [46], was adopted to correlate with the Hubbard correction within the PBESol+ U calculations. The dependence of the lattice parameter on the electronic correlations was also explored considering the LDA [47] and PBE [48, 49] exchange correlations. The periodic solution of the crystal was represented by using Bloch states with a Monkhorst-Pack [50] k -point mesh of $12 \times 12 \times 12$ and 800 eV energy cut-off to give forces convergence of less than $0.001 \text{ eV} \cdot \text{\AA}^{-1}$ and an error in the energy less than 0.5 meV . The spin-orbit coupling (SOC) was included to consider noncollinear magnetic configurations [51]. The phonon calculations were performed within the finite-differences methodology [52, 53] and analyzed through the PHONOPY interface [54]. The modes symmetry was studied with the support of the AMPLIMODES toolkit [55]. Finally, the atomic structure figures were elaborated with the VESTA code [56].

III. RESULTS AND DISCUSSION

As commented before, in the antiferromagnetic antiperovskites where magnetically active (for example Mn and Ni) cations are placed in the octahedral corner sites, a magnetic frustration is produced as a response of the triangular coordination resulting in the octahedral faces. Thus, from the structural point of view, the [111] family of planes form structural Kagome lattices that couples to the resulting magnetic structure after the magnetic frustration is resolved into the symmetry allowed magnetic orderings (*i.e.* Γ_{4g} and Γ_{5g} in our case [19], see Fig. 1(a)). Therefore, by choosing the $\langle 111 \rangle$ direction as the symmetry axis, the resulting noncollinear structure lies in the [111] plane. Then, a strong magnetostructural coupling is expected to be observed in the vibrational landscape of the Mn_3NiN when phonon modes that are entangled to the structural Kagome lattices are involved. The latter interaction is mediated by the magnetic exchange coupling constants and Dzyaloshiinski-Moriya interaction that in turn, depends on the bond's length and bonding angles [57, 58].

As a first step into our analysis, we considered the volume effects, widely reported in the literature [23, 30, 59, 60], in prototype antiperovskite materials such as Mn_3NiN . Moreover, the relationship of the lattice parameter, and associated volume, with the electronic structure in this family of compounds highlights the importance of an appropriate approach to study the spin-phonon coupling (see Fig. 1S in the Supplement Material). As such, aiming to properly map the spin-phonon coupling present in this material, we started by exploring the exchange and correlation effects by studying the influence of different pseudopotentials formalisms on the lattice parameter. This structural parameters directly dependent on the electronic RKKY interaction between the Mn-sites forming the octahedra. Then, we considered LDA, PBE, and PBESol formalisms in this study. We have fixed the magnetic orderings to the noncollinear Γ_{4g} and Γ_{5g} , shown in Fig. 1(a), and then, we proceeded with the full optimization of the electronic structure and the lattice parameters. In both orderings, we obtained, at $U = 0.0$ eV, lattice parameters of 3.648 \AA , 3.830 \AA , and 3.749 \AA for the LDA, PBE, and PBESol, respectively, as included in Fig. 1(b). As expected, the value obtained for PBESol sits in the middle of LDA and PBE formalisms due to their underestimation and overestimation of the lattice parameters, respectively, acknowledged in the field [61].

Experimentally, the observed lattice parameter is $a = 3.886 \text{ \AA}$ at low temperature, below $T_N = 262 \text{ K}$ [30] where the frustrated non-collinear magnetism is present. Interestingly, although the PBESol approach is expected to be well-reproduce in comparison to the experimentally observed value, the obtained parameter is well below the expected by $\Delta a = 0.137 \text{ \AA}$, equivalent to an error of 3.5 %. This disagreement is explained in terms of the strong electronic correlation and the entanglement between the magnetic structure and the volume in this type of com-

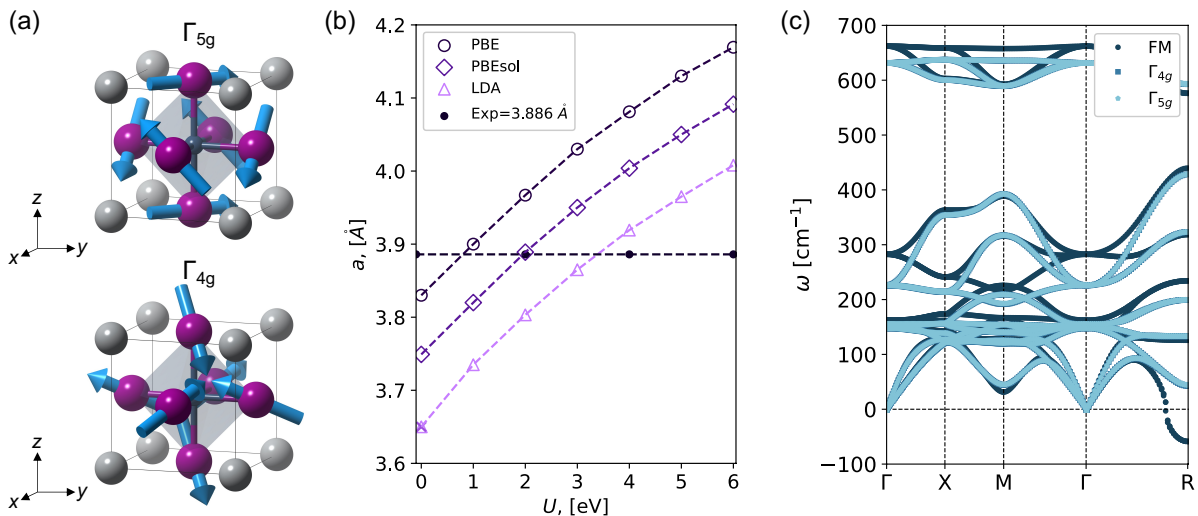


FIG. 1. (Color online) In (a) is presented the Mn₃NiN $Pm\bar{3}m$ structure in which, the Γ_{5g} and Γ_{4g} noncollinear ordering are shown. (b) Lattice parameter as a function of the Hubbard U parameter computed for PBE, PBEsol, and LDA pseudopotentials, respectively. The experimentally included lattice parameter was measured at $T_N = 262$ K below the magnetic transition temperature [30]. (c) Phonon dispersion curves were obtained for the Mn₃NiN at a fixed U value of 2.0 eV and the FM, Γ_{4g} , and Γ_{5g} orderings. The unstable modes are shown at negative frequency values by notation.

pounds. Surprisingly, at the relaxed volume obtained within the LDA approach, the magnetism vanishes and no trace of the magnetic moments is obtained, nor for the Mn-sites, nor for the Ni cell corner sites. Moreover, this relaxed lattice parameter is well below the experimentally obtained above the magnetic transition temperature of $a = 3.888$ Å. In contrast, the net magnetic moments per Mn-atom and noncollinear ordering are obtained when using PBE and PBEsol approaches at the same volume obtained with LDA. Here again, suggesting a strong coupling between the magnetic, electronic, and lattice structure. Therefore, to improve the electronic exchange-correlation misrepresentation, we introduced the DFT+ U approach, in which, the U value was considered for the magnetically active Mn-site that is the main responsible for the magnetostructural response. In Fig. 1(b) we present the lattice parameter values, for the LDA, PBE, and PBEsol, obtained as a function of the on-site Coulomb U value. We observed a rather large expansion for the three considered schemes. For example, for the PBEsol approach, the lattice parameter varies from 3.749 Å to 4.092 Å when the U value is varied from 0.0 to 6.0 eV. This giant expansion of the lattice is due to the strong effect of the electronic structure, and the associated Mn–Mn magnetic exchange, into the structural degrees of freedom possibly influencing the phononic structure. It is worth noticing that, in the LDA calculation for values above $U = 1.0$ eV, the expansion and the increase in the correlation correction favor the appearance of magnetism, and then, a development of a net magnetic moment per Mn atom is clearly observed within the noncollinear antiferromagnetic structure. The latter is along the lines of the expected negative thermal expansion explained in terms of the existence and anni-

hilation of the frustrated magnetic structure as a function of temperature [30]. The observed contraction in the equilibrium volume, in absence of the Hubbard correction, is due to the Mn–Mn overbinding produced by LDA and GGA schemes in metallic Mn-rich compounds [62–64], which in turn, produces a substantial contraction of the lattice parameter, as observed at $U = 0.0$ eV in Fig. 1(b).

After considering a careful characterization of the electronic structure and based-on our previous results aiming to better reproduce the magnetostructural phenomenon and the associated spin-phonon coupling, we have defined the pseudopotential to the PBEsol approach and the on-site correction U value to $U = 2.0$ eV in the PBEsol+ U scheme. Moreover, to correlate and corroborate our theoretical strategy with a more advanced approach, we employed the metaGGA formalism within the SCAN representation [46]. This approach has been successfully applied in the description of metal-transition oxides [65], Mn-rich compounds [64], and metallic Heusler compounds [66]. As such, within the SCAN approach we fully optimized the electronic and structural parameters without the Hubbard correction (*i.e.* $U = 0.0$ eV) and conserving a Γ_{4g} noncollinear magnetic ordering. Under the SCAN representation, we obtained a fully relaxed lattice parameter of $a = 3.863$ Å representing an error of 0.59 % with respect to the experimentally obtained value and the computed lattice parameter for PBEsol+ U , $U = 2.0$ eV. Additionally, we computed the band-structure for the LDA, PBE, PBEsol, and SCAN representation of the exchange-correlation with and without the U correction, shown in Fig. 2S in the Supplement Material. After comparing the electronic structure with the obtained with the SCAN scheme, it can be observed that

the electronic states close to the Fermi energy are considerably improved, for the three schemes, when the on-site Coulomb energy is considered and correctly introduced into the calculations. Nonetheless, the PBEsol+ U offers the advantage of being designed to better reproduce the lattice parameter avoiding computational pressure/strain that could alter the electronic structure. Then, we conclude that the PBEsol+ U methodology fairly reproduces both, the electronic properties and the structural degrees of freedom that might be associated with the vibrational landscape. Interestingly, most of the reports in the literature [9, 21, 29, 67] devoted to this type of compounds do not consider the on-site Coulomb U correction in the exchange-correlation and the cell volume is fixed to the experimentally obtained parameter. The latter approach might be introducing a fictional negative external pressure, which, in turn, could induce differences in the observed properties due to the strong coupling between the magnetic and the atomic structure. Besides, as suggested by Fig. 2S, the electronic structure strongly differs from the one obtained with more advanced methodologies, such as meta-GGA. For this reason, the exchange-correlation correction is needed to better reproduce the electronic structure close to the Fermi energy, and with it, the magnetic response and structural behavior. Thus, the computational and theoretical methodology proposed here is highly recommended when treating this class of compounds.

Once the noncollinear magnetic structure is considered into the symmetry operations, the group symmetry is reduced from the $Pm\bar{3}m$ (SG. 221) space group to the $R\bar{3}m$ (SG. 166) although the point group is conserved to the $\bar{3}m$. The magnetic symmetry groups are defined as $R\bar{3}m'$ (MSG. 166.101) and $R\bar{3}m$ (MSG. 166.97) for the Γ_{4g} , and Γ_{5g} magnetic orderings, respectively, see Fig. 1(a). Next, after carefully having defined the exchange-correlation and the Hubbard correction effects into the electronic and atomic structure, we proceeded by obtaining the full phonon-dispersion curves for the noncollinear FM (111), Γ_{4g} , and Γ_{5g} magnetic orderings, as shown in Fig. 1(c). Due to the metallic character of the Mn_3NiN antiperovskite and the frustrated magnetic structure that is resolved in the non-collinear chiral magnetic Γ_{4g} and Γ_{5g} orderings, we adopted the finite-differences method in which, we considered the non-collinear magnetic ordering at each atomic displacements configuration. The latter displacements are obtained by symmetry into the $2 \times 2 \times 2$ supercell in which the interatomic forces are computed and later used to reconstruct the dynamical matrix tensor and with it, the full phonon-dispersions. In Fig. 1(c) we present the phonon-dispersion curves for the 3 magnetic orderings at the fully relaxed lattice parameter of $a = 3.885 \text{ \AA}$ with $U = 2.0 \text{ eV}$. It is relevant mentioning that despite a symmetry lowering is observed when the noncollinear magnetic orderings are introduced, within the margin error of 2.0 cm^{-1} , the $Pm\bar{3}m$ and $R\bar{3}m$ phonons are indistinguishable. For this reason, the high-symmetry points are selected with respect to the

TABLE I. Phonon frequencies, in cm^{-1} , at the high-symmetry points computed for the Γ_{4g} , Γ_{5g} , and FM orderings and keeping the on-site Coulomb value of $U = 2.0 \text{ eV}$.

Ord. / Ph. mode	Γ_5^-	Γ_4^-	Γ_4^-	Γ_4^-		
Γ_{4g}	149	155	226	631		
Γ_{5g}	148	155	226	631		
FM	151	162	282	662		
	X_1^+	X_1^+	X_5^+	X_3^-	X_1^+	X_5^+
Γ_{4g}	127	155	214	354	600	637
Γ_{5g}	127	155	214	354	600	637
FM	131	162	241	363	603	659
	M_2^+	M_5^-	M_2^-	M_4^+	M_5^-	M_2^-
Γ_{4g}	45	141	193	392	590	636
Γ_{5g}	45	140	193	392	590	636
FM	31	152	216	389	592	657
	R_5^-	R_4^-	R_4^-	R_3^-	R_2^-	R_5^+
Γ_{4g}	43	133	199	324	428	591
Γ_{5g}	44	133	199	323	428	592
FM	-59	126	234	319	440	576

$Pm\bar{3}m$ Brillouin zone, BZ. As it can be appreciated, for the chiral Γ_{4g} and Γ_{5g} noncollinear magnetic orderings, the phonons and vibrations are fully stable along the entire path in the BZ with non-observable tangible differences in the vibrational landscape between them. In contrast, for the FM (111) ordering, a negative (*i.e.* unstable) branch is observed at the R -point. This unstable phonon has a frequency value of $\omega = -59 \text{ icm}^{-1}$. Clearly, this unstable phonon observed, as a result of the magnetic transition between the FM to Γ_{4g} , or Γ_{5g} , is proof of the strong spin-lattice coupling present in this antiperovskite.

In Table I we present the extracted frequency values for the phonons in the Mn_3NiN at the Γ , X , M , and R high-symmetry points. We observed that the frequency values computed for the Γ_{4g} and Γ_{5g} are almost the same in agreement with the degenerated magnetic states. Now, when compared to the FM (111) ordering, we found that several specific modes are highly affected due to the different magnetic orderings. This is the case of the Γ_4^- , X_5^+ , M_2^+ , and R_5^- where the computed $|\Delta\omega|$ values are 56 cm^{-1} , 27 cm^{-1} , 14 cm^{-1} , and 103 cm^{-1} , respectively. After analyzing these modes, we observed that the atomic displacements associated with each of them are related to the Mn-Mn interaction responsible for the magnetic response. In the Γ_4^- case, this mode involves an in-phase octahedral stretching accompanied with a displacement of the nitrogen atoms present in the center of the octahedron. The X_5^+ mode is related with an in-phase stretching involving only the Mn atoms positioned in the equatorial sites of the octahedron alongside with movements of the nitrogen atoms. The case of the M_2^+ mode is also interesting because involves a rigid in-phase octahedral rotation. The most affected mode, the R_5^- , involves a rigid out-of-phase octahedral rotation that conserves the Mn-Mn distance unaffected, as in the M_2^+ case, but, alters the bonding angles inducing a distortion within the

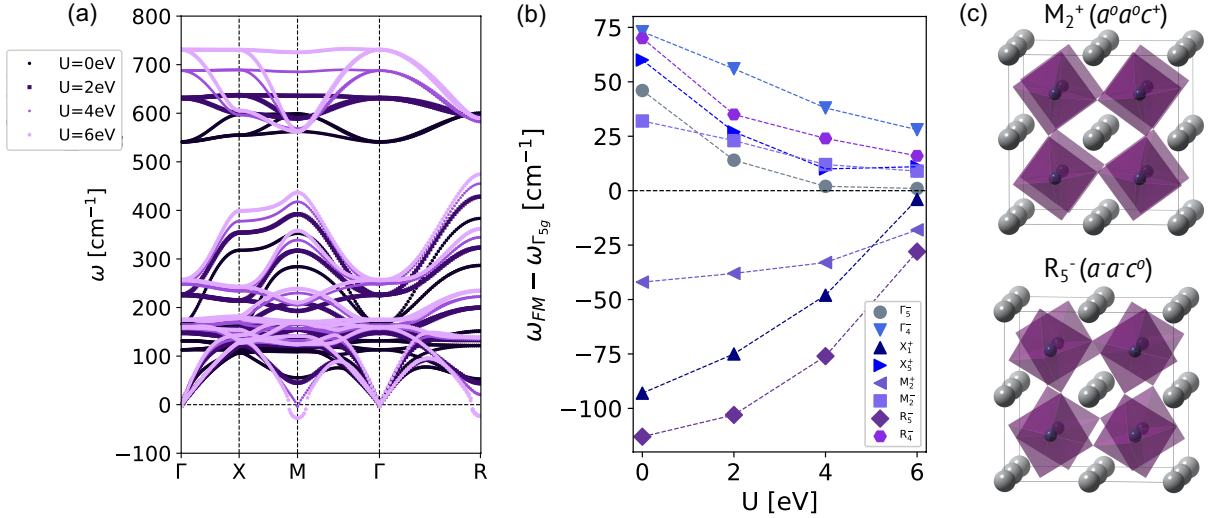


FIG. 2. (Color online) (a) Phonon dispersion for the Γ_{5g} ordering in the Mn_3NiN computed at different U values in which, the lattice volume was fixed to the experimentally obtained value. The latter is in order to explore the effect of the correlation into the vibrational modes. Here, the unstable modes are shown at negative frequency values by notation. (b) Obtained change in the frequencies, $\Delta\omega = \omega_{FM} - \omega_{\Gamma_{5g}}$, when the magnetic transitions are induced. In the latter, the extracted phonon frequencies of the lowest vibrational modes at the high-symmetry points in the Brillouin zone. (c) Representation of the structural distortions associated with the M_2^+ and R_5^- modes where the octahedral rotation and tilting can be appreciated, respectively.

[111] Kagome lattice.

For our next step in the analysis, we studied only the effect of the electronic correlations in the vibrations and the magnetic structure. Then, we fixed the lattice parameters to the relaxed structure within the PBEsol+ U ($U = 2.0$ eV), and then, we vary the U value from 0.0 to 6.0 eV also keeping the Γ_{5g} and FM magnetic orderings fixed. In Fig. 2(a) we present the phonon-dispersion curves obtained at the fixed volume for $U = 0.0, 2.0, 4.0,$ and 6.0 eV considering the Γ_{5g} ordering. Despite the fixed volume, we found that the vibrational modes are strongly affected by the exchange-correlation correction where, in general, a hardening of the branches is observed as the on-site Coulomb term is increased. Interestingly, for values of $U = 6.0$ eV, there is an appearance of two unstable phonons at the M - and R -points. Here, for U values above 4.0 eV, the M_2^+ and R_5^- modes become unstable as a consequence of the large on-site Coulomb repulsion that is affecting the exchange coupling, and in turn, modifying the modes' frequencies. The latter modes are identified as M_2^+ and R_5^- and are representing the in-phase octahedral rotation and the out-of-phase octahedral tilting, respectively, as shown in Fig. 2(c).

In Fig. 2(b) we present the differences, $\Delta\omega = \omega_{FM} - \omega_{\Gamma_{5g}}$, in the phonon frequency, for the most relevant modes close to 0 cm^{-1} . We observe that most of the modes show a tangible influence on the U value. Remarkably, the R_5^- mode experiences a change of 113 cm^{-1} . Interestingly, when the U correction approaches 6.0 eV, the difference in the frequencies between the FM and Γ_{5g} magnetic orderings, starts to decrease considerably, possibly due to an overestimation of the correlation.

Aiming to explore the effect of the on-site Coulomb correction into the volume, and consequently, into the vibrational landscape of Mn_3NiN , we proceeded with the analysis by allowing the volume to relax for the different U values and extracting the phonon-dispersion curves at each relaxed volume, following the procedure explained above. Similarly, the phonons are fully stable for a small regime of U values in the Γ_{5g} and only the M_2^+ and R_5^- modes are strongly affected by the correlation and volume increase. In Fig. 3(a) we present the extracted phonon frequencies for the R_5^- and M_2^+ modes computed within the FM and Γ_{5g} magnetic orderings. As it can be ob-

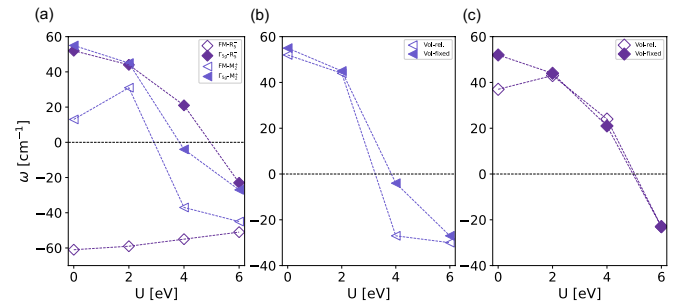


FIG. 3. (Color online) In (a) are presented the M_2^+ and R_5^- phonon frequencies computed at the Γ_{5g} and FM orderings in the Mn_3NiN for different U values in which, the volume relaxation is allowed in the optimization process. Evolution of the M_2^+ and R_5^- frequencies, in (b) and (c) respectively of the Hubbard U value. The M_2^+ (R_5^-) mode is unstable above $U = 4.0$ eV ($U = 6.0$ eV) for both, relaxed and fixed volume, cases.

served, the R_5^- is unstable for the entire regime of U values when the ferromagnetic ordering is fixed. The latter is corroborating that the FM ordering is unstable, independently of the correlation value adopted, and confirms the strong AFM exchange interaction within the Kagome lattice. Interestingly, the M_2^+ becomes unstable, in the FM magnetic ordering for U values above 4.0 eV. In Fig. 3(b), for M_2^+ , and Fig. 3(c), for R_5^- , we present the frequencies obtained for the fixed and relaxed volumes as a function of U by keeping the Γ_{5g} ordering. Here, we noticed that despite the volume changes, the phonon modes hold a similar trend showing an unstable behavior, for both M_2^+ and R_5^- modes, when the U values are above $U = 4.0$ eV.

After analyzing the antiperovskite structure, it becomes clear that the vibrational modes related to rigid octahedral rotations and tilting will be strongly coupled to the magnetic behavior thanks to the magnetic exchange interactions that, in the antiperovskite case, takes place in the Mn–Mn corner-to-corner interaction. As such, the strong magnetic frustration will tend to keep the triangular structure unaffected. However, the hypothetical FM and/or external constrains such as strain, could introduce into the system changes in the electronic structure that could have as a consequence, dislocations of the Kagome lattices formed along with the [111] family of planes thanks to the strong magnetostructural coupling. Therefore, we could expect that induced rotations and tiltings at experimentally growth thin-films, onto substrates with such octahedral patterns, might trigger the ferromagnetic state in the Mn_3NiN antiperovskite.

As observed in the literature for the perovskite oxides counterparts, the strongest spin-lattice coupling phenomenon is observed in manganite-based oxides, such as SrMnO_3 [34–36]. In this manganite oxide, it is possible to achieve a switching in the magnetic structure and to induce phase transitions by external constraints, as it might be obtained in the Mn_3NiN . Thus, in order to disentangle the frustrated lattice contribution and the manganese cation intrinsic tendency to exhibit a large spin-phonon coupling, we performed a computational experiment by computing the lattice parameter dependency on the on-site Coulomb correction in the Fe_3NiN antiperovskite compound. From Fig. 3S, in the Supplement Material, we observe that, although the Fe_3NiN is affected, the influence of the U parameter is smaller, suggesting that the magnetic frustrations in the $A_3\text{BN}$ ($A = \text{Fe}, \text{Mn}, \text{and Ni}$) family are crucial ingredients for the

magnetostructural behavior that it is enhanced by the manganese contribution.

IV. CONCLUSIONS

We have investigated, by means of first-principles calculations, the magnetostructural behavior in the Mn-based nitride Mn_3NiN antiferromagnetic antiperovskite by exploring the spin-phonon coupling. According to our results, we found a rather strong correlation between the magnetic, electronic, and vibrational degrees of freedom. As such, a variation of the phonon frequencies, as well as the cell volume, was observed as a function of the U correlation. Interestingly, phonon modes associated with in-phase and out-of-phase rotations, represented by the M_2^+ and R_5^- respectively, can be tuned by the magnetic ordering in the Mn_3NiN . Remarkably, we highlight the importance of the exchange-correlation treatment in the calculations showing its influence on the electronic, magnetic, and phononic structures. We thus hope that our work will motivate further studies leading to a deeper exploration of the spin-phonon coupling in this antiferromagnetic antiperovskite compound and then, potentially achieving the control of the magnetic features by external constraints, such as epitaxial strain and/or applied magnetic field.

ACKNOWLEDGEMENTS

We thank prof. Aldo H. Romero for helpful comments and discussions. The calculations presented in this paper were carried out using the GridUIS-2 experimental testbed, being developed under the Universidad Industrial de Santander (SC3-UIS) High Performance and Scientific Computing Centre, development action with support from UIS Vicerrectoría de Investigación y Extension (VIE-UIS) and several UIS research groups as well as other funding resources. Additionally, we acknowledge the computational support extended to us by Laboratorio de Supercomputo del Sureste (LNS), Benemérita Universidad Autónoma de Puebla, BUAP, for performing heavy theoretical calculations. A.C.G.C. acknowledge the grant No. 2677 entitled “Quiralidad y Ordenamiento Magnético en Sistemas Cristalinos: Estudio Teórico desde Primeros Principios” supported by the VIE – UIS.

[1] H. Liu and X. Yang, A brief review on perovskite multiferroics, *Ferroelectrics* **507**, 69 (2017).
 [2] M. Fiebig, T. Lottermoser, D. Meier, and M. Trassin, The Evolution of Multiferroics, *Nature Reviews Materials* , 16046 (2016).

[3] N. A. Spaldin, S. W. Cheong, and R. Ramesh, Multiferroics: Past, present, and future, *Physics Today* **63**, 38 (2010).
 [4] N. A. Spaldin and R. Ramesh, Advances in magnetoelectric multiferroics, *Nature Materials* **18**, 203 (2019).

- [5] N. A. Spaldin, Multiferroics: Past, present, and future, *MRS Bulletin* **42**, 385 (2017).
- [6] J. Y. Kim, J.-W. Lee, H. S. Jung, H. Shin, and N.-G. Park, High-efficiency perovskite solar cells, *Chemical Reviews* **120**, 7867 (2020), pMID: 32786671.
- [7] N. Suresh Kumar and K. Chandra Babu Naidu, A review on perovskite solar cells (pscs), materials and applications, *Journal of Materiomics* **7**, 940 (2021).
- [8] T. Wu, Z. Qin, Y. Wang, Y. Wu, W. Chen, S. Zhang, M. Cai, S. Dai, J. Zhang, J. Liu, Z. Zhou, X. Liu, H. Segawa, H. Tan, Q. Tang, J. Fang, Y. Li, L. Ding, Z. Ning, Y. Qi, Y. Zhang, and L. Han, The main progress of perovskite solar cells in 2020–2021, *Nano-Micro Letters* **13**, 152 (2021).
- [9] G. Gurung, D. F. Shao, T. R. Paudel, and E. Y. Tsymbal, Anomalous Hall conductivity of noncollinear magnetic antiperovskites, *Physical Review Materials* **3**, 1 (2019).
- [10] M. Oudah, A. Ikeda, J. N. Hausmann, S. Yonezawa, T. Fukumoto, S. Kobayashi, M. Sato, and Y. Maeno, Superconductivity in the antiperovskite Dirac-metal oxide $\text{Sr}_{3-x}\text{SnO}$, *Nature Communications* **7**, 3 (2016).
- [11] M. Oudah, J. N. Hausmann, S. Kitao, A. Ikeda, S. Yonezawa, M. Seto, and Y. Maeno, Evolution of Superconductivity with Sr-Deficiency in Antiperovskite Oxide $\text{Sr}_{3-x}\text{SnO}$, *Scientific Reports* **9**, 1 (2019).
- [12] B. Wang and K. Ohgushi, Superconductivity in anti-post-perovskite vanadium compounds, *Scientific Reports* **3**, 1 (2013).
- [13] Y. Zhao and L. L. Daemen, Superionic conductivity in lithium-rich anti-perovskites, *Journal of the American Chemical Society* **134**, 15042 (2012), pMID: 22849550.
- [14] J. A. Dawson, T. Famprikis, and K. E. Johnston, Antiperovskites for solid-state batteries: recent developments, current challenges and future prospects, *J. Mater. Chem. A* **9**, 18746 (2021).
- [15] A. C. Garcia-Castro, J. H. Quintero Orozco, and C. J. Paez Gonzalez, Hybrid-improper ferroelectric behavior in $\text{Ba}_3\text{SiO}/\text{Ba}_3\text{GeO}$ oxide antiperovskite superlattices, *European Physical Journal B* **92**, 2 (2019).
- [16] Y. Wang, H. Zhang, J. Zhu, X. Lü, S. Li, R. Zou, and Y. Zhao, Antiperovskites with Exceptional Functionalities, *Advanced Materials* **1905007**, 1 (2019).
- [17] A. C. Garcia-Castro, R. Ospina, and J. H. Quintero, Octahedral distortion and electronic properties of the antiperovskite oxide Ba_3SiO : First principles study, *Journal of Physics and Chemistry of Solids* **136**, 109126 (2020).
- [18] S. V. Krivovichev, Minerals with antiperovskite structure: a review, *Zeitschrift für Kristallographie - Crystalline Materials* **223**, 109 (2008).
- [19] D. Fruchart and E. F. Bertaut, Magnetic Studies of the Metallic Perovskite-Type Compounds of Manganese, *Journal of the Physical Society of Japan*, **44**, 781 (1978).
- [20] D. Boldrin, E. Mendive-Tapia, J. Zemen, J. B. Staunton, T. Hansen, A. Aznar, J.-L. Tamarit, M. Barrio, P. Lloveras, J. Kim, X. Moya, and L. F. Cohen, Multi-site exchange-enhanced barocaloric response in Mn_3NiN , *Phys. Rev. X* **8**, 041035 (2018).
- [21] D. Boldrin, A. P. Mihai, B. Zou, J. Zemen, R. Thompson, E. Ware, B. V. Neamtu, L. Ghivelder, B. Esser, D. W. McComb, P. Petrov, and L. F. Cohen, Giant piezomagnetism in mn_3nin , *ACS Applied Materials & Interfaces* **10**, 18863 (2018), pMID: 29726252.
- [22] P. Lukashev, R. F. Sabirianov, and K. Belashchenko, Theory of the piezomagnetic effect in mn-based antiperovskites, *Phys. Rev. B* **78**, 184414 (2008).
- [23] J. Zemen, Z. Gercsi, and K. G. Sandeman, Piezomagnetism as a counterpart of the magnetovolume effect in magnetically frustrated mn-based antiperovskite nitrides, *Phys. Rev. B* **96**, 024451 (2017).
- [24] E. V. Gomonaj, Magnetostriction and piezomagnetism of noncollinear antiferromagnet Mn_3NiN , *Phase Transitions* **18**, 93 (1989).
- [25] Z. Q. Liu, H. Chen, J. M. Wang, J. H. Liu, K. Wang, Z. X. Feng, H. Yan, X. R. Wang, C. B. Jiang, J. M. Coey, and A. H. Macdonald, Electrical switching of the topological anomalous hall effect in a non-collinear antiferromagnet above room temperature, *Nature Electronics* **1**, 172 (2018).
- [26] H. Tsai, T. Higo, K. Kondou, T. Nomoto, A. Sakai, A. Kobayashi, T. Nakano, K. Yakushiji, R. Arita, S. Miwa, Y. Otani, and S. Nakatsuji, Electrical manipulation of a topological antiferromagnetic state, *Nature*, **1** (2020).
- [27] G. Gurung, D.-F. Shao, and E. Y. Tsymbal, Spin-torque switching of noncollinear antiferromagnetic antiperovskites, *Phys. Rev. B* **101**, 140405 (2020).
- [28] P. X. Qin, H. Yan, X. N. Wang, Z. X. Feng, H. X. Guo, X. R. Zhou, H. J. Wu, X. Zhang, Z. G. G. Leng, H. Y. Chen, and Z. Q. Liu, Noncollinear spintronics and electric-field control: a review, *Rare Metals* **10.1007/s12598-019-01352-w** (2019).
- [29] D. Boldrin, I. Samathrakakis, J. Zemen, A. Mihai, B. Zou, F. Johnson, B. D. Esser, D. W. McComb, P. K. Petrov, H. Zhang, and L. F. Cohen, Anomalous hall effect in noncollinear antiferromagnetic mn_3NiN thin films, *Phys. Rev. Materials* **3**, 094409 (2019).
- [30] M. Wu, C. Wang, Y. Sun, L. Chu, J. Yan, D. Chen, Q. Huang, and J. W. Lynn, Magnetic structure and lattice contraction in Mn_3NiN , *Journal of Applied Physics* **114**, 2 (2013).
- [31] K. Takenaka, Negative thermal expansion materials: Technological key for control of thermal expansion, *Science and Technology of Advanced Materials* **13**, 10.1088/1468-6996/13/1/013001 (2012).
- [32] Z. H. Sun, X. Y. Song, F. X. Yin, L. X. Sun, X. K. Yuan, and X. M. Liu, Giant negative thermal expansion in ultrafine-grained $\text{Mn}_3(\text{Cu}_{1-x}\text{Gex})\text{N}$ ($x = 0.5$) bulk, *Journal of Physics D: Applied Physics* **42**, 10.1088/0022-3727/42/12/122004 (2009).
- [33] X. Song, Z. Sun, Q. Huang, M. Rettenmayr, X. Liu, M. Seyring, G. Li, G. Rao, and F. Yin, Adjustable zero thermal expansion in antiperovskite manganese nitride, *Advanced Materials* **23**, 4690 (2011).
- [34] J. H. Lee and K. M. Rabe, Large spin-phonon coupling and magnetically induced phonon anisotropy in SrMO_3 perovskites ($M = \text{V}, \text{Cr}, \text{Mn}, \text{Fe}, \text{Co}$), *Phys. Rev. B* **84**, 104440 (2011).
- [35] J. Hong, A. Stroppa, J. Íñiguez, S. Picozzi, and D. Vanderbilt, Spin-phonon coupling effects in transition-metal perovskites: A DFT+ U and hybrid-functional study, *Phys. Rev. B* **85**, 054417 (2012).
- [36] J. H. Lee and K. M. Rabe, Epitaxial-strain-induced multiferroicity in srmn_3o_3 from first principles, *Phys. Rev. Lett.* **104**, 207204 (2010).
- [37] P. Hohenberg and W. Kohn, Inhomogeneous electron gas, *Phys. Rev.* **136**, B864 (1964).
- [38] W. Kohn and L. J. Sham, Self-consistent equations including exchange and correlation effects, *Phys. Rev.* **140**,

- A1133 (1965).
- [39] G. Kresse and J. Furthmüller, Efficient iterative schemes for *ab initio* total-energy calculations using a plane-wave basis set, *Phys. Rev. B* **54**, 11169 (1996).
- [40] G. Kresse and D. Joubert, From ultrasoft pseudopotentials to the projector augmented-wave method, *Phys. Rev. B* **59**, 1758 (1999).
- [41] P. E. Blöchl, Projector augmented-wave method, *Phys. Rev. B* **50**, 17953 (1994).
- [42] G. Kresse and D. Joubert, From ultrasoft pseudopotentials to the projector augmented-wave method, *Phys. Rev. B* **59**, 1758 (1999).
- [43] J. P. Perdew, A. Ruzsinszky, G. I. Csonka, O. A. Vydrov, G. E. Scuseria, L. A. Constantin, X. Zhou, and K. Burke, Restoring the density-gradient expansion for exchange in solids and surfaces, *Phys. Rev. Lett.* **100**, 136406 (2008).
- [44] A. I. Liechtenstein, V. I. Anisimov, and J. Zaanen, Density-functional theory and strong interactions: Orbital ordering in mott-hubbard insulators, *Phys. Rev. B* **52**, R5467 (1995).
- [45] J. Sun, M. Marsman, G. I. Csonka, A. Ruzsinszky, P. Hao, Y.-S. Kim, G. Kresse, and J. P. Perdew, Self-consistent meta-generalized gradient approximation within the projector-augmented-wave method, *Phys. Rev. B* **84**, 035117 (2011).
- [46] J. Sun, A. Ruzsinszky, and J. P. Perdew, Strongly constrained and appropriately normed semilocal density functional, *Phys. Rev. Lett.* **115**, 036402 (2015).
- [47] D. M. Ceperley and B. J. Alder, Ground state of the electron gas by a stochastic method, *Phys. Rev. Lett.* **45**, 566 (1980).
- [48] J. P. Perdew, K. Burke, and M. Ernzerhof, Generalized gradient approximation made simple, *Phys. Rev. Lett.* **77**, 3865 (1996).
- [49] M. Ernzerhof and G. E. Scuseria, Assessment of the perdew–burke–ernzerhof exchange–correlation functional, *The Journal of Chemical Physics* **110**, 5029 (1999).
- [50] H. J. Monkhorst and J. D. Pack, Special points for brillouin-zone integrations, *Phys. Rev. B* **13**, 5188 (1976).
- [51] D. Hobbs, G. Kresse, and J. Hafner, Fully unconstrained noncollinear magnetism within the projector augmented-wave method, *Phys. Rev. B* **62**, 11556 (2000).
- [52] K. Kunc and R. M. Martin, Ab initio force constants of gaas: A new approach to calculation of phonons and dielectric properties, *Phys. Rev. Lett.* **48**, 406 (1982).
- [53] P. K. Lam, M. M. Dacorogna, and M. L. Cohen, Self-consistent calculation of electron-phonon couplings, *Phys. Rev. B* **34**, 5065 (1986).
- [54] A. Togo and I. Tanaka, First principles phonon calculations in materials science, *Scr. Mater.* **108**, 1 (2015).
- [55] D. Orobengoa, C. Capillas, M. I. Aroyo, and J. M. Perez-Mato, *AMPLIMODES*: symmetry-mode analysis on the Bilbao Crystallographic Server, *Journal of Applied Crystallography* **42**, 820 (2009).
- [56] K. Momma and F. Izumi, *VESTA3* for three-dimensional visualization of crystal, volumetric and morphology data, *Journal of Applied Crystallography* **44**, 1272 (2011).
- [57] I. Dzyaloshinsky, A thermodynamic theory of weak ferromagnetism of antiferromagnetics, *J. Phys. and Chem. Solid.* **4**, 241 (1958).
- [58] T. Moriya, Anisotropic superexchange interaction and weak ferromagnetism, *Phys. Rev.* **120**, 91 (1960).
- [59] K. Takenaka, M. Ichigo, T. Hamada, A. Ozawa, T. Shibayama, T. Inagaki, and K. Asano, Magnetovolume effects in manganese nitrides with antiperovskite structure, *Science and Technology of Advanced Materials* **15**, 015009 (2014), pMID: 27877651.
- [60] J. Zemen, Z. Gercsi, and K. G. Sandeman, Piezomagnetism as a counterpart of the magnetovolume effect in magnetically frustrated Mn-based antiperovskite nitrides, *Physical Review B* **96**, 10.1103/PhysRevB.96.024451 (2017), arXiv:1512.03470.
- [61] G.-X. Zhang, A. M. Reilly, A. Tkatchenko, and M. Scheffler, Performance of various density-functional approximations for cohesive properties of 64 bulk solids, *New Journal of Physics* **20**, 063020 (2018).
- [62] D. Hobbs, J. Hafner, and D. Spišák, Understanding the complex metallic element mn. i. crystalline and non-collinear magnetic structure of α -mn, *Phys. Rev. B* **68**, 014407 (2003).
- [63] D. Hobbs and J. Hafner, Ab initiodensity functional study of phase stability and noncollinear magnetism in mn, *Journal of Physics: Condensed Matter* **13**, L681 (2001).
- [64] A. Pulkkinen, B. Barbiellini, J. Nokelainen, V. Sokolovskiy, D. Baigutlin, O. Miroshkina, M. Zagrebin, V. Buchelnikov, C. Lane, R. S. Markiewicz, A. Bansil, J. Sun, K. Pussi, and E. Lähderanta, Coulomb correlation in noncollinear antiferromagnetic α -mn, *Phys. Rev. B* **101**, 075115 (2020).
- [65] G. Sai Gautam and E. A. Carter, Evaluating transition metal oxides within dft-scan and SCAN + *u* frameworks for solar thermochemical applications, *Phys. Rev. Materials* **2**, 095401 (2018).
- [66] D. R. Baigutlin, V. V. Sokolovskiy, O. N. Miroshkina, M. A. Zagrebin, J. Nokelainen, A. Pulkkinen, B. Barbiellini, K. Pussi, E. Lähderanta, V. D. Buchelnikov, and A. T. Zayak, Electronic structure beyond the generalized gradient approximation for ni_2MnGa , *Phys. Rev. B* **102**, 045127 (2020).
- [67] V. T. N. Huyen, M.-T. Suzuki, K. Yamauchi, and T. Oguchi, Topology analysis for anomalous hall effect in the noncollinear antiferromagnetic states of Mn_3AN ($A=\text{Ni, Cu, Zn, Ga, Ge, Pd, In, Sn, Ir, Pt}$), *Phys. Rev. B* **100**, 094426 (2019).